"Fast" algorithms for quantum physics

Toshiaki Iitaka
Computer Imformation Center

Introduction

"Fast" algorithms for classical physics require computational efforts proportional to N or $N \log N$ to evaluate all two-body interactions in an ensemble of N particles. in contrast with the traditional methods which require Order(N^2) computational efforts. As a result, large-scale simulations that were previously out of reach can be carried out with reasonable computational efforts.[1)]

Also, "fast" algorithms for quantum physics have been developed in 1990s. These fast algorithms require computational efforts proportional to N or $N \log N$, where N stands for the number of the atoms in the system or the number of the basis functions, to compute the electronic properties in contrast with the conventional Order(N^3) diagonalization methods. As a result, microscopic calculations for very large systems can be carried out with reasonable computational efforts.[2-4)]

In this article we give a brief description of two fast algorithms for the Green's functions and the linear response functions of quantum systems, i.e., the *Particle Source Method* and the *Projection Method*, with their applications to aperiodic systems such as amorphous, liquid, and nanostructure systems. The *Particle Source Method*[5)] has been successfully applied to DC ($\omega = 0$) transport properties of large disordered systems,[6)] and the *Projection Method*[7)] has been used for AC ($\omega \neq 0$) response functions.[8)] Both methods are based on the numerical solution of the time-dependent Schrödinger equation,[9)] use random vectors for calculating the trace and have advantages in implementing on vector-parallel supercomputers. Since these methods do not rely on the locality of the wave functions in contrast to many other fast methods, they have been successfully applied to the phenomena originating from the global coherency of the wave function such as the size effects of nanostructures.[10)]

Particle source method

In many fields of quantum physics, evaluation of the Green's functions[11)] constitutes the most important and demanding part of numerical treatment. Therefore efficient numerical algorithms, such as recursive Green's function methods,[12)] quantum Monte Carlo methods,[13)] the Lanczos[14)] methods, and Forced Oscillator Method (FOM)[15)] have been developed and applied to various problems. In this section we introduce another algorithm (the Particle Source Method; PSM) for calculating the Green's functions that uses numerical solutions of the time-dependent Schrödinger equation with a source term. The PSM can be regarded as a quantum version of the FOM, and is expected to play an important role in computational physics by complementing the quantum Monte Carlo methods and Lanczos methods.

1. Monochromatic particle source Let us introduce the time-dependent Schrödinger equation with an oscillating source term,

$$i\frac{d}{dt}|\phi;t\rangle = H|\phi;t\rangle + |j\rangle e^{-i(\omega+i\eta)t}\theta(t), \tag{1}$$

where the wave function $|\phi;t\rangle$ and an arbitrary source $|j\rangle$ are N-component complex vectors, the Hamiltonian H is an $N \times N$ Hermitian matrix, ω is the frequency of the source, and η is a small positive imaginary part of the frequency. Note that this source term grows up exponentially due to finite η, which simulates *adiabatic switching on* of the particle source. This adiabatic switching on, which has been absent in FOM,[15)] is essential to calculate accurate Green's functions.

The solution of Eq. (1) with the initial condition $|\phi;t=0\rangle = 0$ becomes[11)]

$$|\phi;T\rangle = (-i)\int_0^T dt' e^{-iH(T-t')}|j\rangle e^{-i(\omega+i\eta)t'}, \tag{2}$$

$$= \frac{1}{\omega+i\eta-H}\left(e^{-i(\omega+i\eta)T} - e^{-iHT}\right)|j\rangle, \tag{3}$$

$$\approx \frac{1}{\omega+i\eta-H}e^{-i(\omega+i\eta)T}|j\rangle, \tag{4}$$

$$= G(\omega+i\eta)e^{-i(\omega+i\eta)T}|j\rangle, \tag{5}$$

where we have neglected the second term in the parentheses of Eq. (3). This approximation is justified by using sufficiently long time T satisfying the condition

$$e^{-\eta T} < \delta, \tag{6}$$

where δ is the required relative numerical accuracy of the Green's function. Then multiplying $e^{+i(\omega+i\eta)T}$ on Eq. (5), we obtain the Green's function operated on the ket,

$$|\phi;T\rangle e^{i(\omega+i\eta)T} = G(\omega+i\eta)|j\rangle. \tag{7}$$

2. Impulse-type particle source We can also use an impulse-type particle source,

$$i\frac{d}{dt}|\phi;t\rangle = H|\phi;t\rangle + |j\rangle\delta(t), \tag{8}$$

for calculating the Green's functions. The solution of Eq. (8) with the initial condition $|\phi;t<0\rangle = 0$ becomes

$$|\phi;t\rangle = (-i)e^{-iHt}|j\rangle, \tag{9}$$

which can be computed by solving the homogeneous equation

$$i\frac{d}{dt}|\phi;t\rangle = H|\phi;t\rangle, \tag{10}$$

with the initial condition $|\phi; t=0\rangle = (-i)|j\rangle$. Then the Fourier transformation of Eq. (9),

$$|\tilde{\phi}; T\rangle = \int_0^T dt' |\phi; t'\rangle e^{+i(\omega+i\eta)t'}, \tag{11}$$

$$= (-i)\int_0^T dt' e^{-iHt'}|j\rangle e^{+i(\omega+i\eta)t'}, \tag{12}$$

$$= \frac{1}{\omega+i\eta-H}\left(1-e^{i(\omega+i\eta-H)T}\right)|j\rangle, \tag{13}$$

$$\approx \frac{1}{\omega+i\eta-H}|j\rangle, \tag{14}$$

$$= G(\omega+i\eta)|j\rangle, \tag{15}$$

gives the Green's function operated on the ket. Here we have introduced the imaginary part of the frequency η to neglect the second term in the parentheses of Eq. (13).

The advantage of the impulse-type source over the monochromatic source is that its numerical errors and stability are better understood,[9] and that it can calculate the Green's function for many frequencies at once.

3. $G(\omega - i\eta)$ So far, we have been calculating the Green's function whose frequency has a positive imaginary part. When we need the Green's function whose frequency has a negative imaginary part, $G(\omega - i\eta)$, we should just substitute t by $-t$, and η by $-\eta$ in Eqs. (1) and (8), then follow the procedure described in subsections 1. and 2.

4. Product of the green's functions Since $|j\rangle$ in Eqs. (1) and (8) is an arbitrary ket, we can repeat the calculation of the Green's function by using a new source term $|j_2\rangle = A_1 G(\omega_1 + i\eta_1)|j\rangle$. Then we obtain the product of the Green's functions and operators such as

$$\langle i|A_n G(\omega_n \pm i\eta_n)\cdots A_2 G(\omega_2 \pm i\eta_2) A_1 G(\omega_1 \pm i\eta_1) A_0|j\rangle. \tag{16}$$

It has been very difficult to compute products of Green's functions by using traditional Lanczos Method.

5. Solving the Schrödinger equation To solve the time-dependent Schrödinger Eqs. (1) and (8) numerically, we use the simplest form of the Symmetric Multistep Methods,[9] i.e., the leap frog method,

$$|\phi; t+\Delta t\rangle = -2i\Delta t H|\phi; t\rangle + |\phi; t+\Delta t\rangle \\ -2i\Delta t|j\rangle e^{-i(\omega+i\eta)t}\theta(t), \tag{17}$$

where Δt is the time step. The time step is set as

$$\Delta t = \alpha/E_{max}, \tag{18}$$

where E_{max} is the absolute value of the extreme eigenvalue, and $\alpha \approx 0.1$ is a dimensionless time step. Sample programs of the Symmetric Multistep Methods are available from our web site.

The computational time to calculate $G(\omega + i\eta)$ is estimated by the number N_{prod} of matrix-vector products in the time evolution, which is equal to the integration time T divided by time step Δt,

$$N_{prod} = \frac{T}{\Delta t} = \frac{TE_{max}}{\alpha} = \frac{-\log\delta}{\alpha}\frac{E_{max}}{\eta}, \tag{19}$$

where we used Eq. (6) for the second equality. Note that N_{prod} is independent of the system size N.

6. Random vector A *random vector* is defined by

$$|\Phi\rangle \equiv \sum_{n=1}^{N} |n\rangle \xi_n, \tag{20}$$

where $\{|n\rangle\}$ is the basis set used in the computation and ξ_n are a set of random variables generated by a subroutine, which satisfy the statistical relation

$$\langle\langle\ \xi_{n'}^* \xi_n\ \rangle\rangle = \delta_{n'n}. \tag{21}$$

Here $\langle\langle\ \cdot\ \rangle\rangle$ stands for the statistical average.

This random vector may be also expressed by the eigenstates of H,

$$|\Phi\rangle = \sum_{n=1}^{N} |E_n\rangle \zeta_n. \tag{22}$$

Although we do not know the actual value of ζ_n and $|E_n\rangle$, we can derive the statistical relation of ζ_n as follows. Since Eqs. (20) and (22) are the same vector, we obtain

$$\sum_{m=1}^{N} |E_m\rangle \zeta_m = \sum_{l=1}^{N} |l\rangle \xi_l, \tag{23}$$

$$\sum_{m=1}^{N} \zeta_m^* \langle E_m| = \sum_{l=1}^{N} \xi_l^* \langle l|. \tag{24}$$

By multiplying $\langle E_n|$ on Eq. (23) from left and $|E_n\rangle$ on Eq. (24) from right, ζ_n and ζ_n^* are expressed by a unitary transformation of ξ_l and ξ_l^*

$$\zeta_n = \sum_{l=1}^{N} \langle E_n|l\rangle \xi_l, \tag{25}$$

$$\zeta_n^* = \sum_{l=1}^{N} \xi_l^* \langle l|E_n\rangle. \tag{26}$$

Then the statistical relation of ζ_n is derived as

$$\langle\langle\ \zeta_{n'}^* \zeta_n\ \rangle\rangle = \sum_{l'=1}^{N}\sum_{l=1}^{N} \langle l'|E_{n'}\rangle\langle E_n|l\rangle\ \langle\langle\ \xi_{l'}^* \xi_l\ \rangle\rangle \\ = \sum_{l=1}^{N} \langle E_n|l\rangle\langle l|E_{n'}\rangle \\ = \langle E_n|E_{n'}\rangle = \delta_{n'n}. \tag{27}$$

We can easily notice that the random vector contains all eigenstates of the Hamiltonian with equal probability. Therefore the random vector, Eq. (20), represents the system at a very high temperature ($T \to \infty$).

The statistical average of $\langle\Phi|X|\Phi\rangle$ gives the trace of X

$$\langle\langle\ \langle\Phi|X|\Phi\rangle\ \rangle\rangle = \sum_n \langle\langle\ \zeta_n^* \zeta_n\ \rangle\rangle\ \langle E_n|X|E_n\rangle \\ + \sum_{n\neq n'} \langle\langle\ \zeta_{n'}^* \zeta_n\ \rangle\rangle\ \langle E_{n'}|X|E_n\rangle \tag{28}$$

$$= \sum_n \langle E_n|X|E_n\rangle = \mathrm{tr}\,[X] \tag{29}$$

where we used the statistical relation (27). Note that statistical errors appear when the averages in Eq. (28) are evaluated by the Monte Carlo method.

7. Applications By combining the techniques described in the preceeding subsections, we can calculate various physical quantities, such as the density of states (DOS) $\rho(\omega)$, the DC conductivity σ_{xx}, and the Hall conductivity σ_{xy},[16]

$$\rho(\omega) = \frac{-1}{\pi}\mathrm{tr}\,[\mathrm{Im}G(\omega+i\eta)]$$
$$\sigma_{xx} = \frac{2\hbar}{\pi V}\mathrm{tr}\,[[\mathrm{Im}G(E_f+i\eta)]j_x[\mathrm{Im}G(E_f+i\eta)j_x]]$$
$$\sigma_{xy} = \frac{2B}{\pi cV}\mathrm{tr}\,[\mathrm{Im}\,\{j_xG(E_f-i\eta)j_yG(E_f-i\eta) \times j_xG(E_f-i\eta)j_yG(E_f+i\eta)\}].$$

Figure 1 shows the density of states of silicon crystal consisting of 2^{15} Si atoms in a cubic supercell of 16^3 unit cells. Each unit cell is divided into 8^3 cubic meshes. The energy resolution is $\eta = 0.05$(eV). Three random vectors are used.

Figure 2 compares the DOS of amorphous Fe calculated with PSM and with FOM.[6] Tanaka et al.[17] also calculated the Hall coefficients by using PSM to suggest that the p-d orbital mixture might be the origin of the positive Hall coefficients of liquid Fe.

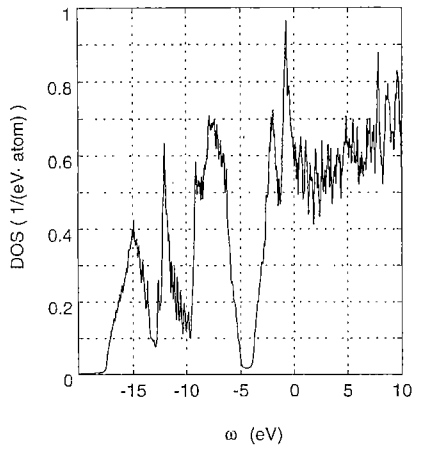

Fig. 1. The density of states of silicon crystal consisting of 2^{15} Si atoms in a cubic supercell of 16^3 unit cells. Each unit cell is divided into 8^3 cubic meshes. The energy resolution is $\eta = 0.05$(eV). Three random vectors are used.

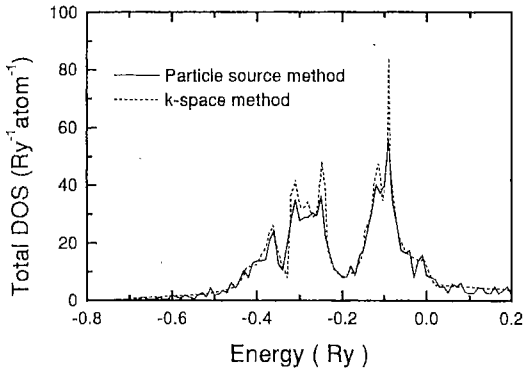

Fig. 2. Comparison of the calculated total DOS for amorphous Fe by using the PSM and the FOM.

Projection method for linear-response

In this section we introduce the Projection Method for linear-response function. First we review a simple derivation of the linear-response function of one-electron system. Second we introduce the projected random vector, which simulates the ground states of a non-interacting many-electron system by a single one-particle wave function. Then, combining these two concepts, we derive a fast algorithm for the linear-response function of a non-interacting many-electron system.

1. One-electron system First, we review the linear-response of a system consisting of a single electron described by the Hamiltonian H. When an impulse of perturbation $A\delta(t)$ is applied to this system, the time evolution of the wave function is described by the Schrödinger equation

$$i\frac{d}{dt}|\phi;t\rangle = \{H + A\delta(t)\}\,|\phi;t\rangle. \tag{30}$$

Note that the impulse $A\delta(t)$ contains all frequency components $Ae^{-i\omega t}$. Assuming that the system was in the initial state $|\phi^{(0)}\rangle$ before the perturbation, the wave function for $t > 0$ becomes

$$|\phi;t\rangle = |\phi^{(0)};t\rangle + |\delta\phi;t\rangle, \tag{31}$$

where

$$|\phi^{(0)};t\rangle = e^{-iHt}|\phi^{(0)}\rangle \tag{32}$$
$$|\delta\phi;t\rangle = (-i)e^{-iHt}A|\phi^{(0)}\rangle. \tag{33}$$

The linear response of an observable B is calculated as

$$\delta B(t) = \langle\phi;t|B|\phi;t\rangle \approx 2\ \mathrm{Re}\langle\phi^{(0)};t|B|\delta\phi;t\rangle \tag{34}$$
$$= 2\ \mathrm{Im}\langle\phi^{(0)}|e^{+iHt}Be^{-iHt}A|\phi^{(0)}\rangle \tag{35}$$

and the Fourier transformation of $\delta B(t)$ gives the linear response to the perturbation $Ae^{-i\omega t}$

$$\chi_{BA}(\omega+i\eta) = \int_0^T dt\ e^{+i(\omega+i\eta)t}\delta B(t), \tag{36}$$

where the imaginary part of frequency η is introduced to limit the integration time to a finite value $T = -\ln\delta/\eta$ with δ being the relative numerical accuracy of Eq. (36).

2. Projected random vector Next, we try to simulate the Fermi degenerated ground state of a non-interacting many-electron system by a single one-particle wave function, and use this wave function to calculate the linear-response function of the system. We define a *projected random vector* by applying the projection operator $\theta(E_f - H)$ to the random vector,

$$|\Phi_{E_f}\rangle \equiv \theta(E_f - H)|\Phi\rangle. \tag{37}$$

The projected random vector may be also expressed by the basis set $\{|E_n\rangle\}$,

$$|\Phi_{E_f}\rangle = \sum_{E_n \le E_f} |E_n\rangle\zeta_n, \tag{38}$$

where E_f is the Fermi energy. Then the statistical average of $\langle\Phi_{E_f}|X|\Phi_{E_f}\rangle$ gives the sum of contributions from each occupied states

$$\langle\langle\ \langle\Phi_{E_f}|X|\Phi_{E_f}\rangle\ \rangle\rangle = \sum_{E_n\le E_f} \langle\langle\ \zeta_n^*\zeta_n\ \rangle\rangle\,\langle E_n|X|E_n\rangle + \sum_{\substack{E_n,E_{n'}\le E_f \\ n\neq n'}} \langle\langle\ \zeta_{n'}^*\zeta_n\ \rangle\rangle\ \langle E_{n'}|X|E_n\rangle, \quad (39)$$

$$= \sum_{E_n\le E_f} \langle E_n|X|E_n\rangle, \quad (40)$$

where we used the statistical relation Eq. (27). Note that statistical errors appear when the averages in Eq. (39) are evaluated by the Monte Carlo method.

3. Many-electron system By introducing the projected random vector, Eq. (38), into $|\phi^{(0)}\rangle$ in Eq. (35) and then into Eq. (36), we obtain our final result, i.e., the linear response of a non-interacting many-electron system,

$$\chi_{BA}(\omega+i\eta) = \left\langle\!\!\left\langle \int_0^T dt\ \ e^{+i(\omega+i\eta)t}\delta B(t) \right\rangle\!\!\right\rangle, \quad (41)$$

where $\delta B(t)$ represents the sum of the response from each electron below the Fermi energy, which is defined by

$$\delta B(t) = 2\ \mathrm{Im}\langle\Phi_{E_f}|e^{+iHt}Be^{-iHt}\theta(H-E_f)A|\Phi_{E_f}\rangle. \quad (42)$$

In Eq. (42), another projection operator $\theta(H-E_f)$ has been introduced to ensure that the excited states should be higher than the Fermi energy.

4. Computational procedure For calculating Eqs. (41) and (42), we start with one realization of the random vector, Eq. (20), and calculate two wave functions,

$$|\phi^{(0)};t\rangle = e^{-iHt}|\Phi_{E_f}\rangle, \quad (43)$$

$$|\delta\phi;t\rangle = e^{-iHt}\theta(H-E_f)A|\Phi_{E_f}\rangle, \quad (44)$$

where the time evolution is calculated by the leap frog method[9] and the projection operators are calculated by the Chebyshev polynomial expansion.[7,8] At each time step, the response, Eq. (42), and its Fourier transformation, Eq. (41), are evaluated. Since the leap frog method and the Chebyshev polynomial expansion consist of the matrix-vector operation $H|\phi\rangle$ whose computational efforts are of Order(N) for sparse Hamiltonians, the total computational effort also becomes of Order(N).

An outstanding advantage of the Projection Method is that it can calculate the linear-response at many frequencies with the CPU time for a single frequency because the most time-consuming calculation, Eq. (42), is common to all frequencies.

Photo-absorption of Si nanocrystallites

Recently the size effects of nanocrystallites on their optical properties attract increasing interest of both theorists and experimentalists.[4,10,18-27] In this section we present the imaginary part of dielectric function $\epsilon(\omega)$ calculated with the Projection method for very large silicon nanocrystallites of size L = 3-8(nm). Nanocrystallites larger than 8(nm) show photo-absorption spectra very similar to bulk spectra, and nanocrystallites smaller than 3(nm) show complicated spectra characteristic to small clusters. In the intermediate region between 8(nm) and 3(nm), peaks in the photo-absorption spectra shift to higher energy and become broader and lower as the crystallite size decreases. In order to explain this size dependence we propose a model based on *the minimum momentum transfer* $q_{min} = \pi/L$, and show that the peak shift is proportional to $1/L^2$.

1. Numerical results In the case of the dielectric function $\epsilon_{\beta,\alpha}(\omega) = 1 + 4\pi\chi_{\beta\alpha}(\omega)$ with $\alpha,\beta = x,y,z$, the perturbation and the response are the external electric field and the polarization, $A = x_\alpha$ and $B = -x_\beta/\Omega$, respectively, where Ω is the volume of the system. In practice we used the formula with the position operators, x_α, replaced by the current operators, j_α, by using partial integration,[8]

$$\epsilon_{\beta\alpha}(\omega+i\eta) = 1 + 4\pi\chi_{\beta\alpha}(\omega+i\eta) \quad (45)$$

$$\chi_{\beta\alpha}(\omega+i\eta) = \left\langle\!\!\left\langle \int_0^T dt\ e^{-\eta t}\frac{\left(e^{+i\omega t}-\delta_{\beta\alpha}\right)}{(\omega+i\eta)^2}K(t) \right\rangle\!\!\right\rangle \quad (46)$$

$$K(t) = \frac{-2}{\Omega}\mathrm{Im}\langle\Phi_{E_f}|e^{+iHt}j_\beta \times e^{-iHt}\theta(H-E_f)j_\alpha|\Phi_{E_f}\rangle \quad (47)$$

Figure 3 shows the dielectric function with energy resolution η = 0.05(eV) of silicon crystal consisting of 2^{15} Si atoms in a cubic supercell of 16^3 unit cells. Each unit cell is divided into 8^3 cubic meshes. One random vector is used. We used the empirical local pseudopotential in reference.[24] The result agrees with experimental results and other theoretical calculations.[28]

Figure 4 shows imaginary part of dielectric function $\epsilon(\omega)$ for (100) $\times$(010) $\times$(001) cubic hydrogenated Si nanocrystallites with various crystal sizes, where each unit cell is divided into 8^3 cubic meshes, the energy resolution is η = 0.05(eV), the vacuum region of width $2a_0$ ($a_0 = 5.43A$ is the lattice constant of Si) is inserted between the nanocrystallite and the boundary of the supercell, and the number of random vectors for statistical average is from 4 to 64 depending on the system size. The empirical local pseudopotential in reference[4] is used.

Figure 5 shows energy shifts of the main peak in optical spectra as a function of the crystal size L/a_0.

2. Effective mass approximation Let us consider the photo-absorption due to the direct transition between two bands $E_j(\mathbf{k})$ and $E_i(\mathbf{k})$. The absorption energy is defined by the difference of the two band energies $\omega_{ij}(\mathbf{k}) = E_j(\mathbf{k}) - E_i(\mathbf{k})$. The absorption spectra of crystals have peaks at the critical points, $\mathbf{k}_{cp}$, where the two bands become parallel, $\nabla E_i(\mathbf{k}_{cp}) = \nabla E_j(\mathbf{k}_{cp})$.[28]

In a crystallite of size L, the wave number is not a good quantum number any more because it fluctuates by $\mathbf{q}_{min} = \pi/L$ according to the uncertainty relation between position and momentum. Therefore the peak energy will shift to

$$\omega_{ij}(\mathbf{k}_{cp}+\mathbf{q}_{min}) = \omega_{ij}(\mathbf{k}_{cp}) + \sum_{n=1}^{3}\alpha_n(\mathbf{q}_{min})_n^2, \quad (48)$$

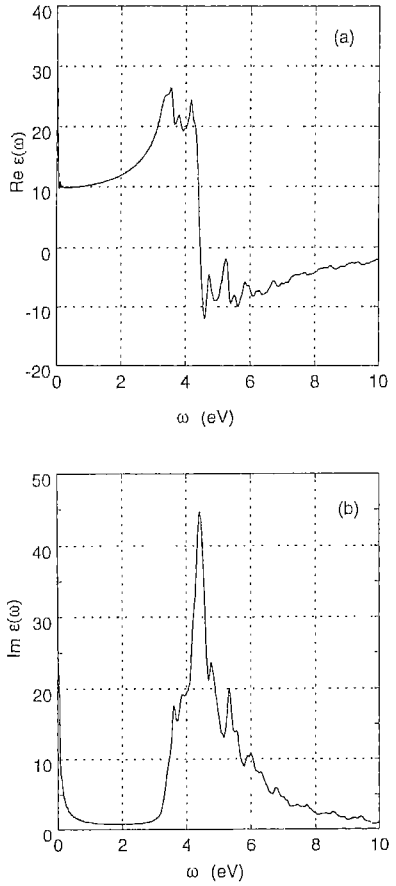

Fig. 3. (a) Re$\epsilon_{xx}(\omega)$ of silicon crystal consisting of 2^{15} Si atoms in a cubic supercell of 16^3 unit cells. Each unit cell is divided into 8^3 cubic meshes. The energy resolution is $\eta = 0.05$ (eV). We used the empirical local pseudopotential in reference.[4] (b) Im$\epsilon_{xx}(\omega)$ of silicon crystal consisting of 2^{15} Si atoms in a cubic supercell of 16^3 unit cells. Each unit cell is divided into 8^3 cubic meshes. The energy resolution is $\eta = 0.05$(eV). We used the empirical local pseudopotential in reference.[4]

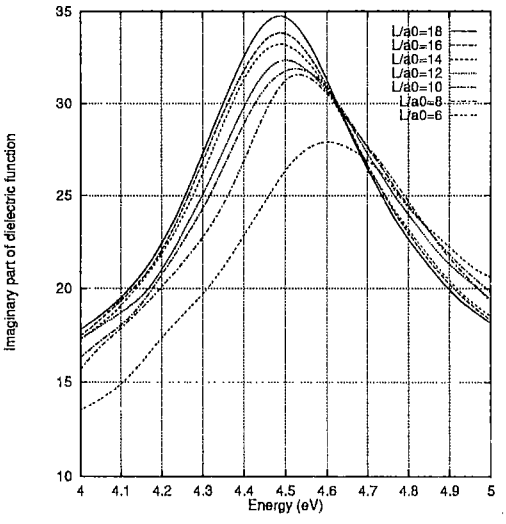

Fig. 4. Imaginary part of dielectric function $\epsilon(\omega)$ for (100) × (010) × (001) cubic hydrogenated Si nanocrystallites with various crystal sizes.

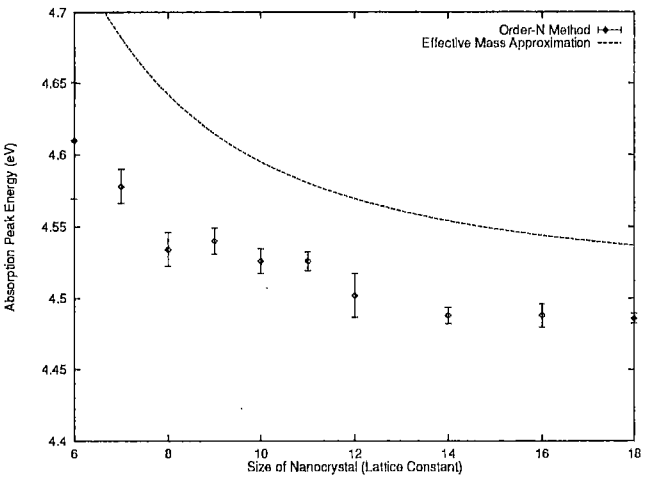

Fig. 5. Energy shifts of the main peak in optical spectra as a function of the crystal size L/a_0.

where α_n are defined by using effective mass at $\mathbf{k} = \mathbf{k}_{cp}$,

$$\alpha_n = \frac{1}{2}\frac{\partial^2 \omega_{ij}(\mathbf{k})}{\partial \mathbf{n}^2}\bigg|_{\mathbf{k}=\mathbf{k}_{cp}}. \tag{49}$$

Therefore the peak shift is proportional to $q_{min}^2 \propto 1/L^2$. The dashed line in Fig. 5 shows the peak energy estimated by Eq. (48).

3. Si amorphous-nanocrystallite system According to the recent numerical calculations[10] and experimental measurement,[27] Si nanocrystallite embedded in amorphous silicon atoms (a-nc system) shows the size effects in optical absorption spectra. In this case the energy shift may be interpreted in terms of momentum fluctuation caused by the scattering of electron in the amorphous part of the system. Although the mean potential is almost the same for amorphous and nanocrystallite region

$$\overline{\Delta V(\mathbf{r})} = \langle \mathbf{k}|\Delta V|\mathbf{k}\rangle = \frac{1}{\Omega}\int d\mathbf{r}\Delta V(\mathbf{r}) \approx 0,$$

electrons are scattered in the amorphous region by the deviation from the crystal potential

$$\Delta V(\mathbf{r}) = V_{\text{amorphous}}(\mathbf{r}) - V_{\text{crystal}}(\mathbf{r}) \neq 0,$$

and cause the momentum fluctuation. When the amorphous region is thin enough, the wave function $|\mathbf{k}; a - nc\rangle$ of a-nc system may be expanded by the unperturbed crystal wave functions in the same band with wave number near $\mathbf{k}$

$$|\mathbf{k}; \text{a-nc}\rangle = |\mathbf{k}\rangle + \sum_{\mathbf{k}'\neq\mathbf{k}} |\mathbf{k}'\rangle \frac{\langle \mathbf{k}'|\Delta V|\mathbf{k}\rangle}{E(\mathbf{k}) - E(\mathbf{k}')} + \cdots,$$

and this fluctuation causes the shift of peak energy in the same way as in isolated nanocrystallites.

4. Size effects of plasmon frequency An electron passing through a film of nanocrystallites may excite plasmons with probability proportional to Im $\epsilon^{-1}(\omega)$. The energy loss of the electron will exhibit characteristic quantized plasmon loss when the dielectric function pass through the zero.[28]

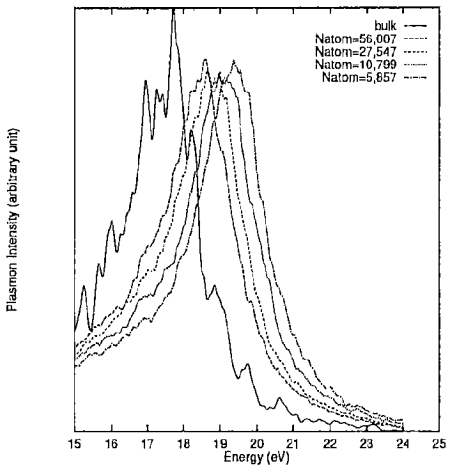

Fig. 6. The imaginary part of inverse dielectric function, Im $\epsilon^{-1}(\omega)$ of Si nanocrystallites of various sizes.

Figure 6 shows the imaginary part of inverse dielectric function, Im $\epsilon^{-1}(\omega)$, of Si nanocrystallites of various sizes. The fine structures in the spectra are mainly caused by the statistical errors due to a small number of randomvectors. The size effects of plasmon energy is much larger than that of photo-absorption spectra, and may be easily observed by the electron energy loss spectroscopy.

5. Summary In this section we studied the size effects of Si nanocrystallites on their photo-absorption spectra by using the Projection Method. The results show that the peak shift of nanocrystallites larger than 3(nm) can be explained by the minimum momentum transfer model. This knowledge would give us a way to measure size of nanocrystallites by measuring photo-absorption spectra.[26]

$\sigma(\omega)$ in Anderson model

The Anderson Hamiltonian can be written as

$$H = \sum_{\mathbf{R}} \epsilon_{\mathbf{R}} |\mathbf{R}\rangle\langle\mathbf{R}| - V \sum_{\mathbf{R},\delta\mathbf{R}} |\mathbf{R}\rangle\langle\mathbf{R}+\delta\mathbf{R}| \tag{50}$$

where $\epsilon_{\mathbf{R}}$ is the site energy distributed uniformly in the range $[-(W/2)V, +(W/2)V]$, and $\delta\mathbf{R}$ are the displacement vectors to nearest neighbors on a simple cubic lattice.

The frequency dependent conductivity for a non-interacting electron gas with spin is calculated by the *Projection Method*[8]

$$\sigma(\omega+i\eta) = \left\langle\!\!\left\langle \int_0^T dt\; e^{-\eta t} \frac{\left(e^{+i\omega t}-1\right)}{i(\omega+i\eta)} K(t) \right\rangle\!\!\right\rangle_{\epsilon_{\mathbf{R}},\,\Phi} \tag{51}$$

$$K(t) = \frac{-2}{\Omega}\mathrm{Im}\langle\Phi_{E_f}|e^{+iHt} j_x \times e^{-iHt}\theta(H-E_f) j_x|\Phi_{E_f}\rangle \tag{52}$$

where j_x and $\theta(X)$ are the current operator and the projection operator, respectively. Here $\langle\langle\ \cdot\ \rangle\rangle_{\epsilon_{\vec{R}},\Phi}$ stands for the statistical average over random site energies and random vectors. An advantage of the Projection Method with the Anderson Hamiltonian is that the statistical averaging over random site energies and over random vectors can be computed simultaneously because they are statistically independent.

Figures 7, 8, and 9 shows $\sigma(\tilde{\omega})$ as a function of the normalized frequency $\tilde{\omega} = \rho(0)\omega$ for a cube of size $L = 14, 30, 256$, respectively. The disorder is set to $W/V = 14.9$, which is supposed to be close to the Anderson transition point.[29-33] The conductivity $\sigma(\tilde{\omega})$ of each system shows the theoretically predicted frequency dependence[30] $\tilde{\omega}^{1/3}$ in a wide frequency range. The calculated conductivity deviates from the theoretical behavior at high and low frequencies. The deviation at high frequency originates from finite band width of the model Hamiltonian. The deviation at low frequency originates from the finite system size or the finite imaginary part of the frequency, η.

The detailed study of the critical disorder and the exponent will be published elsewhere.[34]

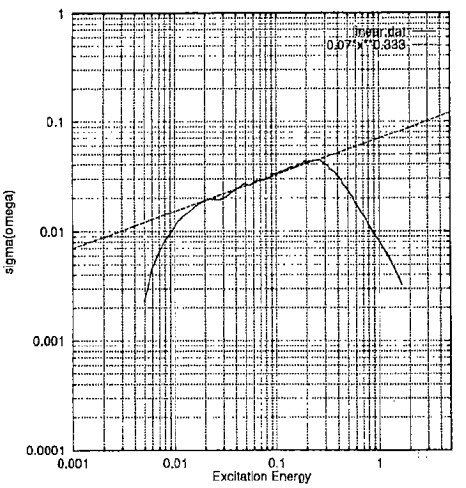

Fig. 7. Dynamical conductivity $\sigma(\tilde{\omega})$ as a function of the normalized frequency $\tilde{\omega}$ for a cube of size $L = 14$ with the disorder $W/V = 14.9$.

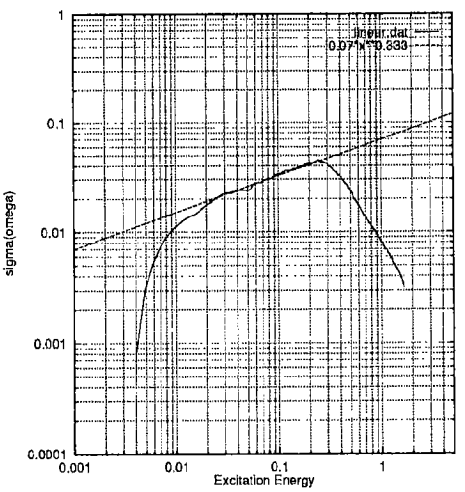

Fig. 8. Dynamical conductivity $\sigma(\tilde{\omega})$ as a function of the normalized frequency $\tilde{\omega}$ for a cube of size $L = 30$ with the disorder $W/V = 14.9$.

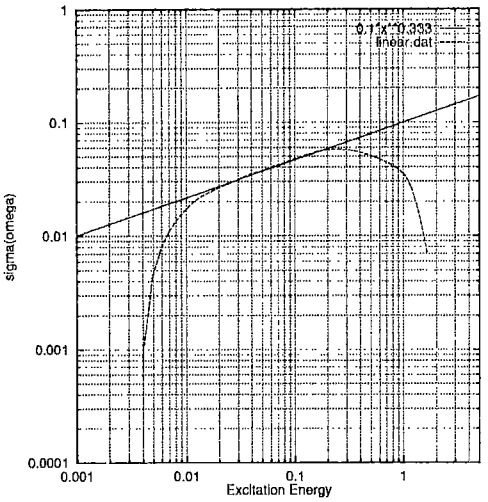

Fig. 9. Dynamical conductivity $\sigma(\tilde{\omega})$ as a function of the normalized frequency $\tilde{\omega}$ for a cube of size $L = 256$ with the disorder $W/V = 14.9$.

Anomalous quantum dynamics for eigenvalues

As the advancement of high performance computers, the importance of numerical solution of the time-dependent Schrödinger equation has been increasing. However, a straightforward application of conventional algorithms in library routines such as Runge-Kutta method simply fails because of their numerical instabilities. Therefore many authors have been trying to find efficient stable algorithms for the time-dependent Schrödinger equation. Among them, we proposed a class of conditionally stable algorithms named as the *Symmetric Multistep Methods*, and studied their numerical errors and stability in detail.[9)]

In the preceding sections we solved the time-dependent Schrödinger equation by using the *leap frog method*, the simplest form of the Symmetric Multistep Methods, within its stability condition $\alpha \equiv |E_{max}\Delta t| < 1$. If we use the leap frog method with $\alpha > 1$, the numerical solution diverges exponentially. Although this diverging solution does not correspond to any real physical process and has been regarded as an obstacle to cope with, we have found a way to exploit this anomalous quantum dynamics to extract eigenvalues and eigenvectors efficiently from large-scale Hermite matrices.[35)]

This method can be regarded as a quantum version of the Okamoto-Maris method to compute eigenvalues and eigenvectors by using diverging solutions of the classical equations of motion of harmonic osccilators.[36)]

Summary

We have developed two types of Order(N) algorithms for the Green's functions and the linear-response functions, that is, the *Particle Source Method* and the *Projection Method*. These algorithms make it possible to calculate the optical and transport properties of various large systems that have been impossible by conventional schemes. In this article, we have briefly described the basic idea of these two methods by illustrating their effectiveness with numerical applications to quantum nanostructures and Anderson models.

I would like to thank to S. Nomura, H. Hirayama, X. Zhao, Y. Aoyagi, T. Sugano, N. Carjan, D. Strottman, A. Mitsutake, Y. Okamoto, T. Ebisuzaki, H. Tanaka, M. Arai, H. Shima, T. Nakayama, M. Suzuki, and Y.H. Ohtsuki for their discussions, support and/or collaboration.

References

1) L. Greengard: Science **265**, 909 (1994).
2) P. Ordejon, D. A. Drabold, M. P. Grumbach, and R. M. Martin: Phys. Rev. B **48**, 14 646 (1993); P. Ordejon, D. A. Drabold, R. M. Martin, and M. P. Grumbach: Phys. Rev. B **51**, 1456 (1995); P. Ordejon, E. Artacho, and J. M. Soler: Phys. Rev. B **53**, 441 (1996).
3) E. Hernandez, M. J. Gillan, and C. M. Goringe: Phys. Rev. B **53**, 7147 (1996); E. Hernandez, M. J. Gillan, and C. M. Goringe: Phys. Rev. B **55**, 485 (1997); C. M. Goringe, E. Hernandez, M. J. Gillan, and I. J. Bush: Comput. Phys. Commun. **102**, 1 (1997).
4) L. W. Wang: Phys. Rev. B **49**, 154 (1994); L. W. Wang and A. Zunger: Phys. Rev. Lett. **73** 1039 (1994).
5) T. Iitaka: High Performance Computing in RIKEN 1995, p. 241 (1996).
(http://www.riken.go.jp/lab-www/nanoelectronics/iitaka/)
(http://espero.riken.go.jp/)
6) H. Tanaka: Phys. Rev. B **57**, 2168 (1998).
7) O. F. Sankey, D. A. Drabold, and A. Gibson: Phys. Rev. B **50**, 1376 (1994).
8) T. Iitaka et al.: Phys. Rev. E **56**, 1222 (1997); T. Iitaka: Phys. Rev. E **56**, 7318 (1997).
9) T. Iitaka: Phys. Rev. E **49**, 4684 (1994); T. Iitaka, N. Carjan, and D. Strottman: Comput. Phys. Commun. **90**, 251 (1995); T. Iitaka: *Introduction to Computational Quantum Dynamics*, (Maruzen, Tokyo, 1994), (in Japanese).
10) S. Nomura et al.: Phys. Rev. B **54**,13974 (1996); S. Nomura et al.: Phys. Rev. B **56**, 4348 (1997); S. Nomura et al.: Mat. Sci. Eng. B **51**, 146 (1998).
11) E. N. Economou: *Green's Functions in Quantum Physics*, (Springer-Verlag, New York, 1983).
12) P. A. Lee and D. S. Fisher: Phys. Rev. Lett. **47**, 882 (1981); D. J. Thouless and S. Kirkpatrick: J. Phys. C **14**, 235 (1981); A. MacKinnon: Z. Phys. B **59**, 385 (1985).
13) R. N. Silver, J. E. Gubernatis, and D. S. Sivia: Phys. Rev. Lett. **65**, 496 (1990); For a review see, e.g., *Quantum Monte Carlo Methods in Condensed Matter Physics*, edited by M. Suzuki, (World Scientific, Singapore, 1993); W. Linden: Phys. Rep. **220**, 53 (1992); E. Y. Loh and J. E. Gubernatis: in *Electronic Phase Transitions*, edited by W. Hanke and Yu. V. Kopaev, (Elsevier, Amsterdam, 1992), p. 177.
14) C. Lanczos: J. Res. Nat. Bur. Stand. **45**, 255 (1950); **49**, 33 (1952); For a review see, e.g., D. W. Bullet, R. Haydock, V. Heine, and M. J. Kelly, in *Solid State Physics* edited by H. Erhenreich, F. Seitz, and D. Turnbull (Academic, New York, 1980), Vol. 35; E. Dagotto, Rev. Mod. Phys. **66**, 763 (1994).
15) M. L. Williams and H. J. Maris: Phys. Rev. B **31**, 4508 (1985); K. Yakubo, T. Nakayama, and H. J. Maris: J. Phys. Soc. Jpn. **60**, 3249 (1991); T. Terao, K. Yakubo, and T. Nakayama: Phys. Rev. E **50**, 566 (1994); For a review see, e.g., T. Nakayama, in *Computational Physics as a New Frontier in Condensed Matter Research* edited by H. Takayama, M. Tsukada, H. Shiba, F. Yonezawa, M. Imada, and Y. Okabe, (Physical Society of Japan, Tokyo, 1995) and references therein.
16) M. Itoh: Phys. Rev. B **45**, 4242 (1992).
17) H. Tanaka and M. Itoh: in preparation.
18) See, for example, *Porous Silicon Science and Technology*, edited by J.-C. Vial and J. Derrien (Springer and Les Edition de Physique, Berlin, 1995).
19) K. A. Littau et al.: J. Phys. Chem. **97**, 1224 (1993).
20) S. Hayashi and K. Yamamoto: J. Lumin. **70**, 352 (1996).
21) X. Zhao et al.: Phys. Rev. B **50**, 18654 (1994).
22) M. V. Rama Krishna and R. A. Friesner: Phys. Rev. Lett. **67**,

629 (1991).
23) F. Huaxiang, Y. Ling, and X. Xide: Phys. Rev. B **48**, 10978 (1993).
24) L. W. Wang and A. Zunger: J. Chem. Phys. **100**, 2394 (1994).
25) A. Zunger and L. W. Wang: Appl. Surf. Sci. **102**, 350 (1996).
26) S. Komuro: private communication.
27) X. Zhao: private communication.
28) M. L. Cohen and J. R. Chelikowsky: *Electronic Structure and Optical Properties of Semiconductors*, 2nd ed. (Springer-Verlag, Berlin, 1988).
29) A. Singh and W. L. McMillan: J. Phys. C **17**, 2097 (1985).
30) F. J. Wegner: Z. Physik **25**, 327 (1976).
31) A. MacKinnon and B. Kramer: Phys. Rev. Lett. **47**, 1546 (1981).
32) P. Lambrianides and H. B. Shore: Phys. Rev. B **50**, 7268 (1994).
33) H. Shima and T. Nakayama: Meet. Abstracts Phys. Soc. Jpn. Vol. 53, p. 670 (1998).
34) T. Iitaka: in preparation.
35) A. Mitsutake, T. Iitaka, and Y. Okamoto: Comput. Phys. Commun. **96**, 217 (1996).
36) Y. Okamoto and H. J. Maris: Comput. Phys. Commun. **76**, 191 (1993).